ORIGINAL ARTICLE



Numerical modeling on wave-current flows and bed shear stresses over an algal reef

Yi-Ru Lan¹ · Zhi-Cheng Huang^{1,2}

Received: 4 May 2023 / Accepted: 6 June 2024 / Published online: 1 July 2024 © The Author(s) 2024

Abstract

Currents in coastal zones under multiple mechanisms in terms of tides, waves, wind, and high roughness are difficult to model; bed shear stresses under wave-current flows are particularly challenging yet not being well studied. Few studies reported the modeling and validation of the bed shear stress in reef environments. In this paper, we present the first direct assessment of numerical modeling on depth-averaged currents and bed shear stresses over an algal reef using a coupled wave-current model (Delft-3D). The modeled results were validated and compared to the field observed data. The model considers hydrodynamic forcing in terms of tides, waves, wind stresses, and bed friction. Results show that the model generally reproduces the depth-averaged currents and bed shear stresses when considering all the mechanisms. Two numerical cases with and without wind forcing were tested to examine the effects of the winds. We found that the tide is mostly the primary factor driving the current, even in shallow waters within a depth of 3 m; however, the currents are also significantly affected by wind speeds and wind directions during high-wind events. When the wind direction is in the same direction as the tidal current, the current speed increases, suggesting the importance of the wind stress on the coastal currents. In addition, two models were chosen to study the nonlinear enhancement of bed shear stress by waves. We found a significant difference between the two models in predicting the bed shear stresses compared to the observed data. Nonlinear contribution from wave enhances the magnitude of bed shear stresses, which reduces the model error. The results highlight the nonlinear interaction between waves and currents is meaningful in predicting the bed shear stresses during high-wave-orbital motions; improvement of the present wave-current nonlinear interaction model for predicting the bed shear stresses may be needed.

Keywords Current · Bed shear stress · Wind · Wave–current interaction · Delft-3D

Graduate Institute of Environmental Engineering, National Central University, Taoyuan City, Taiwan



[☑] Zhi-Cheng Huang zchuang@ncu.edu.tw

Graduate Institute of Hydrological and Oceanic Sciences, National Central University, Taoyuan City, Taiwan

1 Introduction

The hydrodynamic processes in shallow water conditions accompanied by rough reef bed boundary layer especially tend to become much more complex and difficult to predict, while this kind of nearshore area is also closely related to human economic and social activities, as well as the ecosystem for marine organisms. Currents in coastal zones play a primary role in various processes of nearshore reef systems, including sediment transport [14], delivery of larvae [26], and the transport and dispersal of heat and substances, such as nutrients and oxygen [9, 45]. Coastal currents in reef systems can be driven by various forcing mechanisms, including tides, waves, wind, and bed friction. The relative importance of each mechanism may vary across different coastal environments, resulting in spatial and temporal differences in coastal currents [42].

Wind force exerts on the free surface of the water as wind stress, developing changes in both flow and wave motions on the upper layer of the water column [2]. Studies on the effects of the wind on wave fields have been attained through laboratory experiments and numerical models (e.g., [52]). As for the flow field, wind effects may be neglected in some studies since the wind stresses act on the boundary layer of the upper water column and have a secondary impact on the depth-averaged currents. However, the currents can be shaped by winds significantly or even dominantly for the whole water column in very shallow waters and more sheltered regions, such as lagoons in reefs [20, 44]. Waves are found to affect the coastal currents in many physical processes, such as the spatial gradient of radiation stress that causes a gradient of water level and, therefore, drives the nearshore current [3, 32] and wave-current nonlinear interaction [56]. Waves have been found to play a dominant role in circulations on reefs in many studies [18, 36, 46, 64].

The bed friction causes the bottom drag and creates a bottom boundary layer (BBL) to alter the velocity profile of the coastal currents [43]. Wave BBL affects the wave motions by various processes, such as shoaling, depth-refraction, and dissipation [39]. Typically, waves coexist with coastal currents and create wave-current interactions [16], and wave-current interaction has been an important process in BBL as it induces additional momentum transfer [13, 15, 38]. The seabed on reefs is rougher with morphological complexity than a sandy bed; therefore, it forms a BBL with higher bottom drag and turbulent mixing [1, 42]. As a result, the flow and wave fields in reef systems are typically much more complex than those on sandy beaches. Bed shear stress is studied for the reef BBL and is associated with energy dissipation [23] and the corresponding turbulence fluxes of heat and suspended sediment [58]. The bed shear stress in the wave-current boundary layer can be expressed by a quadratic drag law for mean current and enhanced nonlinearly by wave orbital velocity. The nonlinear enhancement of bed shear stress by waves needs to be better understood in field, laboratory, and modeling studies [31, 53, 60, 66]. The dependence of bed shear stress on roughness and hydrodynamic motion could be well established empirically on uniform fixed sand [49, 58], but the stress becomes more unpredictable if the bottom condition is more complicated and rougher.

Numerical models have been proposed to study current circulation and wave fields on reefs. Some studies have focused on the response of the hydrodynamics to the tidal forcing in reef systems [17, 33]. Several modeling studies have described hydrodynamic motions under the effects of both wind and tides [12, 37] and waves and tides [59]. Considering that the relative importance of the various forcing mechanisms in



reefs may vary in different environments, models with interactions of tides, wind, and waves have been included in many studies [18, 35, 47]. While the coastal currents have been studied, few studies reported the modeling and variation of bed shear stress in reef environments.

It is difficult to numerically model the coastal currents under the complex interaction between winds, waves, and currents. The modeling and validating of the more critical hydrodynamic parameters, bed shear stresses, is even more challenging, leading to the bed shear stresses over reefs needing to be better understood in field, laboratory, and modeling studies. We apply a numerical model that considers the hydrodynamic forcing of tides, waves, and wind to study the depth-averaged currents and bed shear stresses over an algal reef on the Taoyuan coast. We test the skill of the model to reproduce the depth-averaged currents, wave heights, and bed shear stresses on the rough reef platform. The questions this paper aims to study are (1) to assess the influence of wind forcing on the coastal currents, (2) to understand the performance of the existing model to predict the bed shear stress, and (3) to explore how the wave-current interaction affects the bed shear stress on the reef.

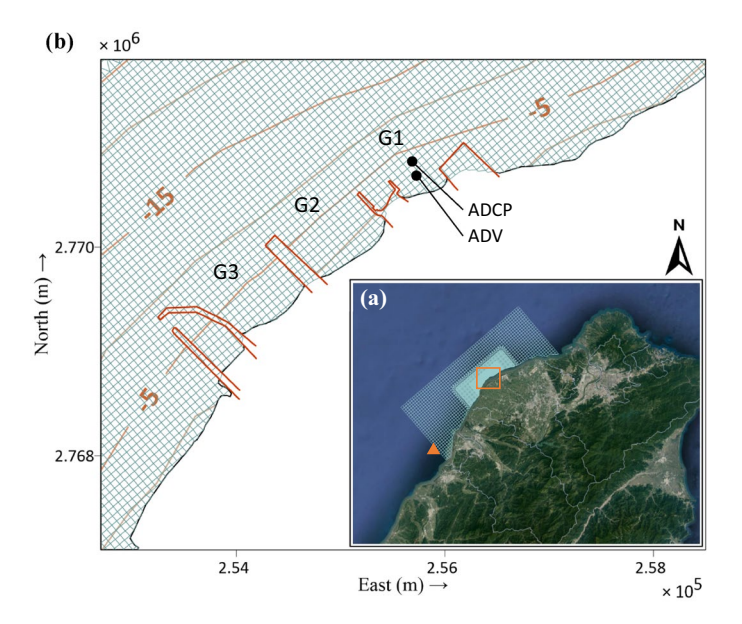


Fig. 1 Study area and computational grids. **a** Satellite image of Taoyuan coast from Google Earth, with the whole computational grids of Delft3D Flow module. Orange triangle: the location of the Hsinchu Buoy. **b** detailed view of model grids with bathymetry contours of the domain specified by the orange rectangle in (**a**), where black dots: instrument sites of ADCP and ADV. Red polygon: coastal jetties along the shoreline. In this model, these four jetties were treated as objects that blocks flow exchange between two adjacent computational cells



2 Methods

2.1 Site description

The study site is located in the Taoyuan coastal area on the northwestern part of Taiwan main island (Fig. 1). The Taoyuan coast (Fig. 1) faces the Taiwan Strait with an alongshore span of approximately 40 km. Approximately 27 km of reefs are found on the Taoyuan coastline; the reef extends to the sea from the land area to a water depth of about 10 to 20 m. The reef is called an "algal reef" because it is mainly formed by crustose coralline algae instead of corals. These reefs are mainly created by coralline algae, providing habitat for a diverse algal-reef ecosystem along the coast [65]. The reefs are protected and have been declared a marine protected area (Guanxin Algal Reefs Wildlife Refuge) due to the presence of unique endemic species and corals [28].

The instruments were deployed in a shallow water with a depth ranging from 0 to 3 m. The intertidal zone is divided by four coastal jetties into three zones (G1, G2, and G3), as shown in Fig. 1. Most in-situ field observations were conducted in the G1 area because conservation class organisms and significant changes in topography are found at G1 and G2. A long-term project was initiated in 2019 to measure waves and suspended sediment concentrations [29].

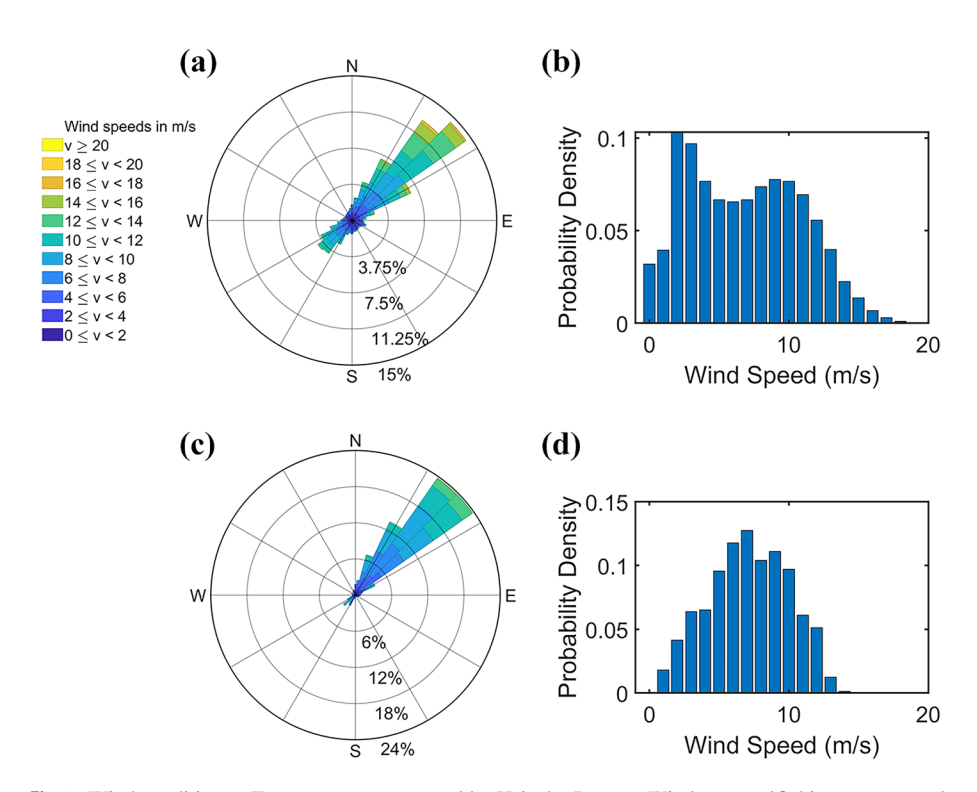


Fig. 2 Wind condition at Taoyuan coast measured by Hsinchu Buoy. a Wind rose and b histogram recording during 2010–2020. c Wind rose and d histogram recording during model period of case W1. The two wind roses share the same color legend



The tide in the Taoyuan coast is dominated by the semidiurnal and mixed diurnal tide; the mean tidal range is 3.5 m and the spring and neap tidal ranges reach up to 4 m and 2 m, respectively. Taoyuan coast is located in Monsoon Asia and experiences southwesterly monsoon winds from May to August with wind speeds of around 5 m/s while northeasterly monsoon winds from October to March with wind speeds of around 10 m/s [5]. Wind patterns for the entire year on the Taoyuan coast are summarized in Fig. 2a, which shows that the dominant wind direction is northeast at 45 degrees, while winds from the southwest with lower speeds play a secondary role.

2.2 Field measurements

Instruments were deployed to measure various hydrodynamic parameters, including tides, waves, currents, and turbulence, along with suspended sediment properties such as sediment concentrations, particle sizes, and distributions (not shown here for brevity). An acoustic Doppler current profiler (ADCP, Nortek signature 1000) was deployed at a low-low-water position, located 4 m below sea level and 350 m seaward from the coastline. The ADCP continuously measured the waves and currents with hourly bursts of 4096 samples at 4 Hz since April 2021. Data of ADCP in the period of 2022/04/25 to 2022/05/25 were analyzed. Bed shear velocity was measured using an array of four 6 M-Hz acoustic Doppler velocimetries (ADV, Nortek Vector) near the ADCP from 2022/04/25 to 2022/05/25. The ADVs were set to sample flow velocities hourly at 16 Hz for 16,384 samples, i.e., hourly burst measurement of 17.67 min. The velocities were converted into eastward, northward, and vertical velocities from the measured azimuth and tilt angles. The instrument sites are shown in Fig. 1.

The measured instantaneous velocity vector by ADVs, \mathbf{u} , is decomposed into a mean component $(\overline{\mathbf{u}})$, a wave-induced component $(\widetilde{\mathbf{u}})$, and a turbulent component (\mathbf{u}') as follows:

$$\mathbf{u} = \overline{\mathbf{u}} + \widetilde{\mathbf{u}} + \mathbf{u}',\tag{1}$$

where $\mathbf{u} = (u, v, w)$, $\overline{\mathbf{u}} = (\overline{u}, \overline{v}, \overline{w})$, $\tilde{\mathbf{u}} = (\tilde{u}, \tilde{v}, \tilde{w})$, and $\mathbf{u'} = (u', v', w')$. The mean velocity component, $\overline{\mathbf{u}}$, is determined by taking the time average over a 17.67-min duration of instantaneous velocity data. The differencing technique with the adaptive least-square filter proposed by Shaw and Trowbridge [51] is used to separate the components of the wave-induced velocities and the turbulent velocities. In this method, we assume that the coherent signals in the vertical direction are generated by wave motion, while the incoherent signals are attributed to turbulent fluctuations. We analyze two velocity time series from the four Acoustic Doppler Velocimeters (ADVs) to separate turbulence. The wave-induced velocity at position 1 is estimated from the filtered velocity, \hat{u}_1 , which is defined as

$$\hat{u}_1(t) = \int_{-L/2}^{L/2} \hat{h}(t - \tau) u_2(t) d\tau, \tag{2}$$

where t is time, L is the selected filter length, \hat{h} is the filter weight, and u_2 is the velocity measured at position 2. A least-square filter is then used to determine \hat{h} :

$$\hat{\mathbf{h}} = (\mathbf{A}^{\mathrm{T}} \mathbf{A})^{-1} \mathbf{A}^{\mathrm{T}} \mathbf{u}_{1} \tag{3}$$

Here **A** is an $M \times N$ windowed data matrix for the velocity at position 2, where M is the number of data points, N is the number of filter weights, and \mathbf{u}_1 is the velocity vector at



position 1. The wave-induced velocity vector at position 1, \hat{u}_1 , was estimated by convolving the matrix **A** with \hat{h} :

$$\hat{\mathbf{u}}_1 = \mathbf{A}\hat{\mathbf{h}}.\tag{4}$$

The velocity vector of the turbulent component at position 1 is then computed as follows:

$$\mathbf{u}'(t) = \mathbf{u}(t) - \overline{\mathbf{u}}_1 - \hat{\mathbf{u}}_1(t). \tag{5}$$

Quality control and ogive curve testing (OgT) were performed to ensure the data quality of the measured turbulent fluctuation and Reynolds stresses [22, 25]. Error analysis on the velocity and turbulence measurements are given in appendix A.

2.3 Model description

We used a coupled flow-wave model developed by Deltares (Delft 3D) to reproduce the currents and wave fields in the study area. The hydrodynamic motion was simulated using D-Flow FM (Flexible Mesh) module over a layer of unstructured grid in two-dimensional mode. In the two-dimensional mode, modeling is conducted with the application of a depth-averaged approach under the unsteady shallow-water assumption and the Boussinesq approximation [10, 30]. Under these assumptions, vertical accelerations are not taken into account and the vertical profile of the velocity is not resolved, which brings out the depthaveraged currents obtained by solving the conservation equations of mass and momentum in the horizontal direction. Tidal variation was set at the open boundaries with wind stress input and bottom roughness. The model considers the effects of bed and wind shear stresses acting at the sea bottom and the water surfaces. The bed and wind shear stresses are treated as external sources of the momentum in the momentum equation. Bed shear stresses were expressed by a quadratic drag $\text{law}\tau_b = -\rho C_{d,cur} \|U\|U$, where the friction coefficient $C_{d.cur} = gn^2/h^{1/3}$ is formulated by Manning [40], with h is the water depth, and n is the Manning coefficient. A Manning coefficient of 0.03 is used in this study. Wind forcing was modeled as a shear stress $\tau_{wind} = C_{d,wind}\rho_a \|U_{10}\|U_{10}$, where ρ_a is the density of air, U_{10} is the wind speed at 10 m above the free surface, and $C_{d,wind}$ is the wind drag coefficient. The values of the wind drag coefficient depending on wind speeds were defined by Yelland et al. [63]. The values of the wind drag coefficient $C_{d,wind}$ depending on wind speeds were inputted using the formula proposed by Yelland et al. [63], which was measured in the open ocean. In contrast to deep water, $C_{d,wind}$ in shallow water has been studied less, and may be a little higher than in deep water [6, 50]. We note that the inputted $C_{d,wind}$ may be approximately 5 to 10% smaller when using Yelland et al. [63]'s formula compared to those derived in shallow water, particularly in wind speeds ranging from 5 to 12 m/s. Some studies conducted in shallow waters also adopt $C_{d,wind}$ values from formulas developed for open ocean conditions (e.g., [41]).

The simulation of wind-generated, random, and short-crest waves was conducted by using the D-Waves module based on the third-generation SWAN (Simulating Waves Nearshore). More details for the model description and wave coupling can be found in Deltares [11]. Depth-limited wave breaking was set with the criterion of γ =0.5. Bottom friction was described using the friction model proposed by Madsen et al. [39], with a prescribed equivalent Nikuradse roughness, k_w , of 0.2 m and a wave friction factor using the



empirical formula proposed by Swart [57]. The wave frictional factor is functional to the near-bed flow velocity and seabed roughness [43].

The input values of n and k_w affect the bed stresses caused by waves and mean currents. These stresses are closely linked to the physical length scale of seabed bottom roughness. The standard deviation of seabed elevation measured by the lidar system as reported by Huang et al. [24], σ_b , is approximately 7.5 ± 1.4 cm on the reef. Reasonable estimates of wave friction factors and dissipation of wave height over reefs are achieved when the value of k_w is set as 2 to 4 times σ_b [23, 34]. This results in k_w ranges from 0.15 to 0.3 m, indicating a reasonable setting of $k_w = 0.2$ m in this study. The values of k_w yield apparent hydraulic roughness, $z_0 = k_w/30$, ranging from 0.005 to 0.01. Considering a water depth ranging from 1 to 3 m, the values of k_w yield a commonly wall-law defined drag coefficient of mean current $C_{d,cur} = \left\{0.41/\left[1 + \ln(z_0/h)\right]\right\}^2$, ranging from 0.0058 to 0.0129. This indicates a reasonable choice of Manning's n value as 0.03, which gives $C_{d,cur} = gn^2/h^{1/3}$, ranging from 0.0061 to 0.0088 for water depths between 1 and 3 m.

Bed shear stresses are subject to both current and wave motions, and the nonlinear wavecurrent interactions contribute to the enhancement of the bed shear stresses. This complex and nonlinear process was described in many different methods. An algebraic approximation using parametric fitting coefficients to the methods was derived by Soulsby [54], and implemented in the D-Waves module. The time-mean bed shear stress (τ_m) and maximum bed shear stress (τ_{max}) in the parameterization of Soulsby are of the form:

$$\left|\tau_{m}\right| = Y(\left|\tau_{c}\right| + \left|\tau_{w}\right|),\tag{6}$$

$$|\tau_{\text{max}}| = Z(|\tau_c| + |\tau_w|),\tag{7}$$

with $Y = X\{1 + bX^p(1 - X)^q\}$, $Z = 1 + aX^m(1 - X)^n$, and $X = |\tau_c|/(|\tau_c| + |\tau_w|)$. τ_c is bed shear stress due to current along, and τ_w is bed shear stress due to waves along. It is obvious that the bed shear stresses driven by both waves and currents are not merely superpositions of τ_c and τ_w , but nonlinear combinations by the parameters Y and Z. Parameters a, b, p, q, m, and n, which determine the value of Y and Z, vary with different methods. Each wave-current interaction method has its own fitting parameters. The values of these parameters and more detailed information are given in Appendix B. Two wave-current interaction models were chosen to study the variation of bed shear stress and the nonlinear contribution of bed shear stress from waves.

2.4 Model domain and configuration

Two-dimensional flow fields were calculated on a layer of unstructured grids in the flow module. The grids cover the entire Taoyuan coast with a resolution from 1000 m at the three open boundaries and refined to 50 m approaching the shore, as shown in Fig. 1. The southwestern boundary coincided with the location of the Hsinchu buoy. The Hsinchu buoy is at a location of approximately 6.4 km offshore and at a water depth of 24.5 m. The use of unstructured grids performs a good fit to the coastline smoothly. For a wave module, a two-grid system (1000 m and 50 m) was used, and both were structured grids because of the unavailability of unstructured grids in D-Waves. Bathymetry data were obtained from two sources: (1) the field measurement data (about 350 m horizontal resolution) for the nearshore area along the Taoyuan



coast, provided by the Water Resource Agency of Taiwan, and (2) the bathymetry map (about 1 km horizontal resolution) retrieved from General Bathymetry Chart of the Ocean (GEBCO).

The model was performed from 25th April to 25th May, which corresponds to the measurement period of the instruments. In addition to the land boundary on the coast, there are three open boundaries in the flow modules: an offshore boundary and two lateral boundaries, as shown in Fig. 1. The three open boundaries were set in the flow module with tidal data of 14 dominant tidal constituents obtained from the fully global model of ocean tides, TPXO8-atlas. Hourly wind and wave data measured by the Hsinchu buoy were used as input boundary conditions for the modeling. The wind is assumed as a uniform wind field across the computing domains in both the flow and wave modules with inputs of wind magnitude and wind direction for all the computing grids. The three open boundaries were set in the wave module with hourly data of significant wave height, wave direction, and peak wave period.

3 Results and discussions

3.1 Model validation and comparison

The performance of the model to reproduce the currents, wave heights, and wave directions was tested against the field data. To quantify the comparison between model predictions (X_{simu}) and observations (X_{obs}) , a measure of model skill [61] was defined as:

$$skill = 1 - \frac{\sum \left| X_{simu} - X_{obs} \right|^2}{\sum \left(\left| X_{simu} - \overline{X_{obs}} \right| + \left| X_{obs} - \overline{X_{obs}} \right| \right)^2}, \tag{8}$$

where the overbar indicates time averaging over the period of modeling. The parameter ranges from 0 to 1, and a value of 1 and 0 stands for perfect agreement and complete disagreement between model predictions and field observations.

Field observed depth-averaged currents were compared with the model results at the site of ADCP in G1, as shown in Fig. 3. The comparison of current velocities in the eastern and northern directions suggests that the current patterns are well reproduced with high skill levels of 0.84 to 0.91. The modeled significant wave heights also show satisfied agreement with field observations, though slight over-predictions appear at peak values. Water levels and wave directions are both accurately reproduced with very high skill values of 0.99. The time series of the current data oscillates with tides. The spectral analysis also shows significant peak values at tidal harmonics (not shown here). The results indicate that the coastal current is mainly driven by tidal forcing even at the shallow water depth of 3 m in G1. The current flows southwest during flooding tides, while the current turns northeast during ebbing tides. In addition, the waves came from the north at most of the time. As shown by the time-series data of wind and waves (Fig. 3a), wind speeds were notably higher in two periods: (1) 30th April to 3rd May, and (2) 14th May to 17th May. Winds from the northeast direction with speeds of about 10 to 15 m/s occurred continuously during these periods, resulting in a significant strengthening of the southwestern currents.



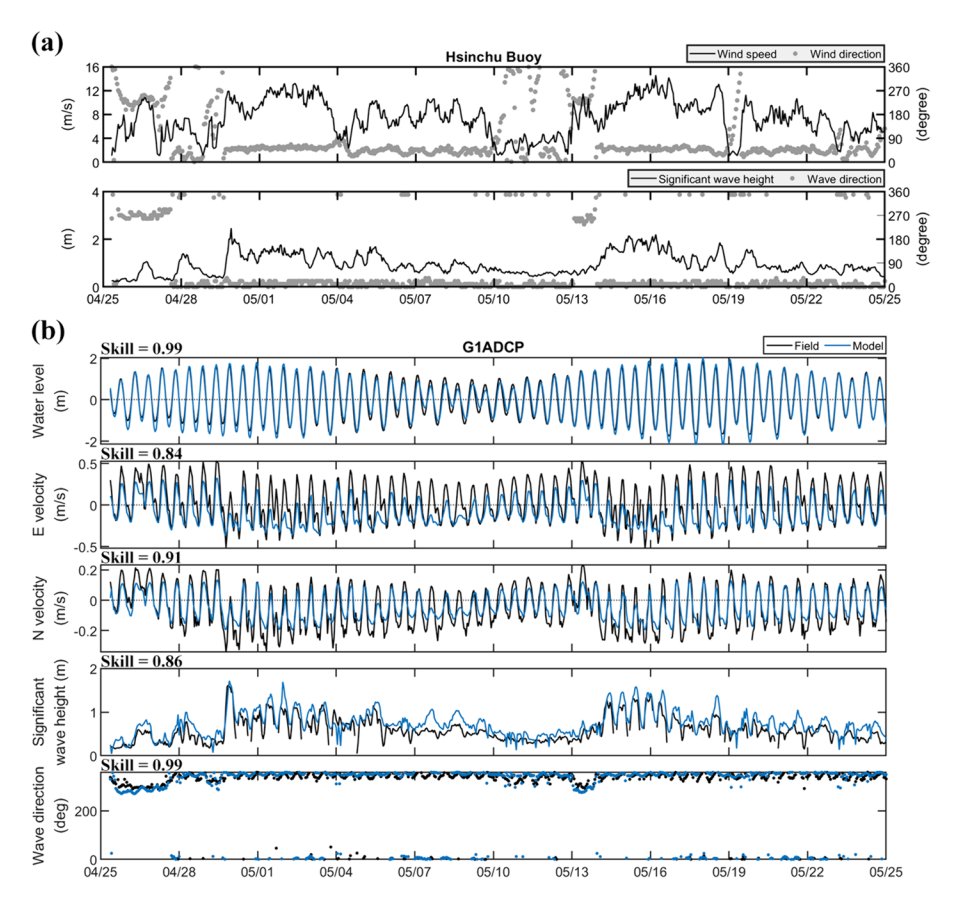


Fig. 3 a top panel: wind speed and direction; bottom panel: significant wave height and wave direction measured by Hsinchu buoy. **b** Comparison between field observations and model results, where the E velocity indicates the eastward flow velocity, and the N velocity indicates the northward flow velocity. The model skill are marked in each panels

Table 1 Summary of model settings and results for different wind conditions

Case	Duration	Wind forcing	Model skill			
			Current velocity E-W component	Current velocity N-S component		
W1	2022/04/25-2022/05/25	On	0.84	0.91		
W2	2022/04/25-2022/05/25	Off	0.88	0.86		

3.2 Effects of wind forcing

Two scenarios (W1 and W2) were modeled to assess the effect of wind forcing on the coastal currents. The model settings of the two scenarios are summarized in Table 1. The modeling period is from 25th April to 25th May 2022, with or without wind forcing for



Fig. 4 Comparison between observed and modelled current magnitude (U) for case W1. Colorbar is the current direction (direction in going to)

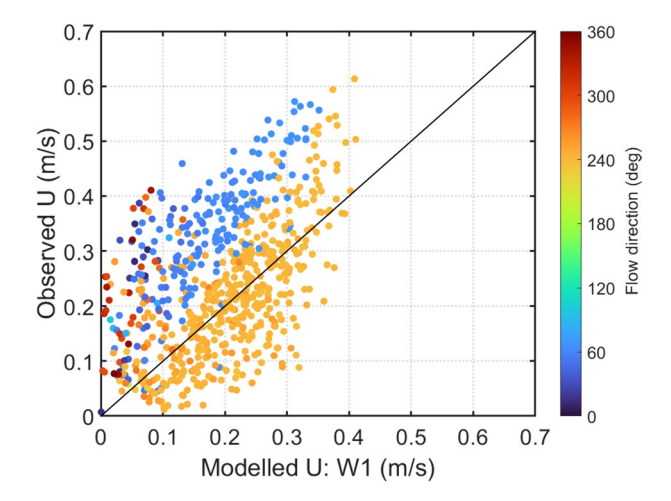
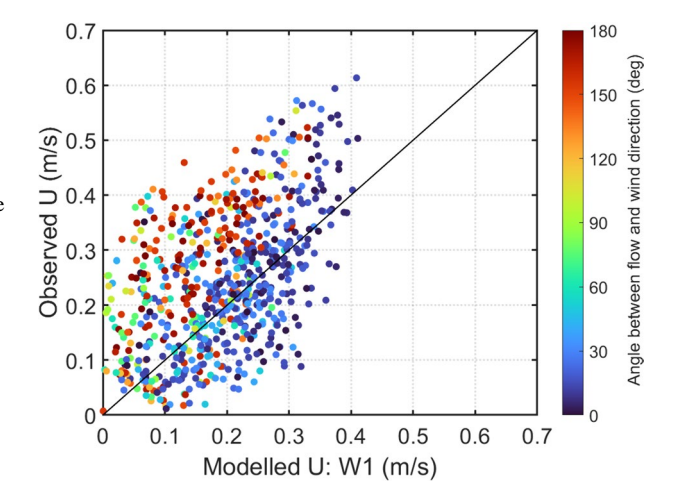


Fig. 5 Comparison between observed and modelled current magnitude (U) for case W1. Colorbar is the angle between current and wind directions, where the 0 and 180 degrees represent that the wind direction is the same and opposite with the flow direction, respectively



cases of W1 and W2. The wind blew dominantly from the northeast at around 45 degrees. Figure 4 shows that the accuracy of the modeled current magnitude is highly associated with the current direction. The model reproduces the observed current well when the direction is at approximately 240°, representing flooding tides. In addition, when the current goes in the direction of around 60° during ebbing tides, the model tends to underpredict the current velocity. The wind stress generates upper surface current boundary layer and wind-driven current [62]; higher mean shear and turbulence production might be expected when the wind goes opposite with the tidal current, and therefore alters the tidal currents [7, 8, 19, 48].

Figure 5 shows that the currents with the same direction of winds tend to have higher values, while the current magnitude is slower when the currents go oppositely with the winds. The effects of the wind on the depth-averaged currents depend on wind speeds and directions, as shown in the case W1, where the northeastern wind dominates. The skill values of these two scenario models are summarized in Table 1. The skill values of W2



are similar to those of W1. The current of the east—west component is slightly better reproduced for case W2, while the current of the north—south component is better reproduced for case W1. The comparison between the two cases with and without wind forcing indicates that the coastal currents at a water depth of 3m are significantly affected by winds. The angle difference between the wind and the current also affects the depth-averaged currents; the current speed decreased by winds when the current goes oppositely to the wind, while the current speed increases when the current and wind are in the same direction.

Comparisons between the observed and modeled results reveal that the performance of the model prediction is related to the current direction, which corresponds to the tidal phase. The coastal currents going southwestward during flooding tides are well reproduced. However, the currents going northeastward during ebb tides tend to be underpredicted. This discrepancy between flood and ebb tides may be caused by the coarse resolution of the bathymetric measurement, the low resolution of the computational grids, and coastal jetties in the adjacent sea. The coastal currents in shallow waters are particularly susceptible to bathymetry, while the bathymetry measurement often becomes much more difficult and inaccurate in shallower regions. The imperfect measurement and poor resolution of topographic elevations may cause errors in model prediction and have also been reported in several studies on modeling the hydrodynamics over reefs [18, 47]. The model used here ignored the nonlinear interaction between the wind-driven and tidal currents while some studies have found that the nonlinear effects of wind on tidal currents are an important factor (e.g., Holmedal and Wang [21],Jacob and Stanev [27],Ruessink et al. [48]). More studies and numerical testing are needed to clarify these issues.

3.3 Bed shear stress

Two wave-current interaction methods were chosen to study the variation of bed shear stress and the nonlinear contribution of bed shear stress from waves. The model proposed by Grant and Madsen (1979) (hereafter, GM79), which gave a good all-around performance [55], is implemented in the combined wave-current models in Delft3D. In addition, we used another model proposed by Bijker [4] (hereafter BK67) to increase the nonlinear contribution of bed shear stress from waves. Two models, GM79 and BK67, which take account of nonlinear enhancement from waves with different combinations of parameters, carry out different Y and Z and therefore yield different magnitudes of enhancement throughout X. According to the approximation of Soulsby [54], when X become smaller (around <0.3), BK67 has larger Y than GM79, which means that BK67 obtains a larger nonlinear enhancement of the bed shear stress than GM79 when τ_w is relatively larger. By comparing the results from these two models, how the nonlinear wave-current interaction

 Table 2
 Summary of model settings and results for different methods of wave-current interaction methods

Case	Wave-current interaction model	Model skil			
		Bed shear velocity	Current velocity E-W component	Current velocity N-S component	Current magni- tude
GM79	Grant and Madsen (1979)	0.37	0.84	0.91	0.67
BK67	Bijker [4]	0.51	0.72	0.76	0.54



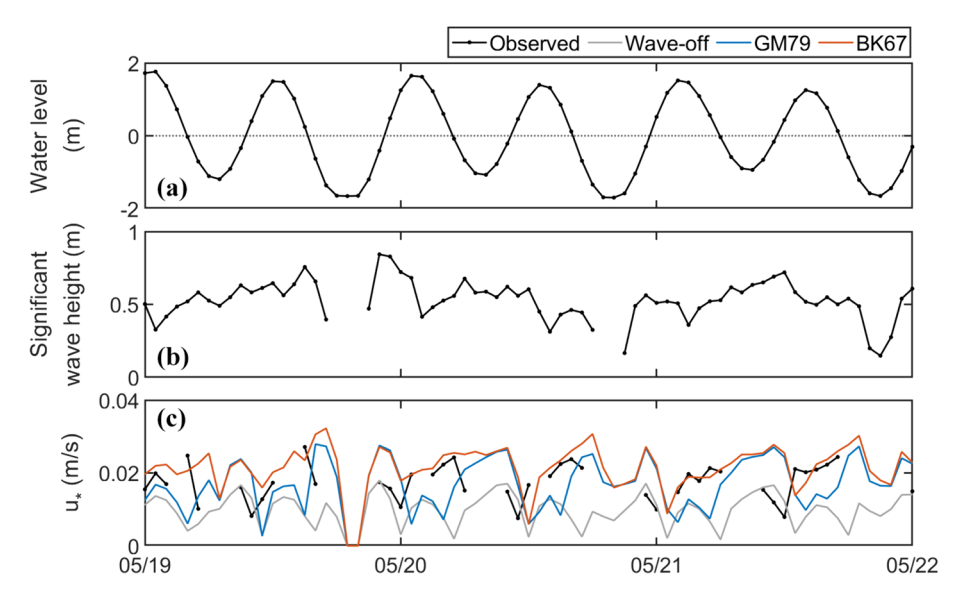


Fig. 6 Comparison between observed and modelled results, where u_* indicates the shear velocity. **a** time series of water level, **b** significant wave height and **c** u_* . Notes that only period from 2022/05/19 to 2022/05/22 are shown for easily seen

affects the bed shear stress on the reef could be investigated. The model settings of these two models are summarized in Table 2.

The model results are shown in Fig. 6, and the skill values are summarized in Table 2. Here, the modeled bed shear velocities u_* were derived from shear stresses using the equation, $\tau_m = \rho u_*^2$, where ρ is water density. The results are compared with the field measurements obtained by the ADV array. The model predicts generally well on both the magnitude, trends, and variability of the bed shear velocities. Figure 6(a) shows that the observed shear velocity mainly varies in phase with the tide and is modulated by wave. This variability in time can be well captured by both the two models. However, there are discrepancies in magnitude between the observation and model result from GM79, leading to a low skill value of 0.36. On the other hand, bed shear velocities modeled by BK67 are partially enhanced, making noticeable differences between the model results of GM79 and BK67.

More detailed comparisons of the model results are given in Fig. 7. Differences between the model results of GM79 and BK67 are particularly noticeable. Model GM79 underpredicts or overpredicts the shear velocities, while model BK 67 provides good agreements for some data points. The skill value improves to 0.51 when the BK67 model has been applied. When assessing based on skill value, it appears that model BK67 performs better in predicting bed shear stresses, and GM79 performs better for reproducing current speed; however, we were unable to evaluate the performance regarding modelled bed shear stress and current speed separately. Increased wave bed shear stress is generated at higher waves, further contributing to the total bed shear stress of the wave-current interaction flow, therefore resulting in a reduction in the current speed. To discuss the effects of waves, we performed a scenario case excluding the wave module. The modeled bed shear velocity is shown in Fig. 6(c), marked in gray color. The mean value of the modeled shear velocity without effects of waves is 0.009 m/s, which is notably smaller than the measured value of 0.018 m/s, as well as the modeled values of 0.018 m/s using GM79 and 0.021 m/s using



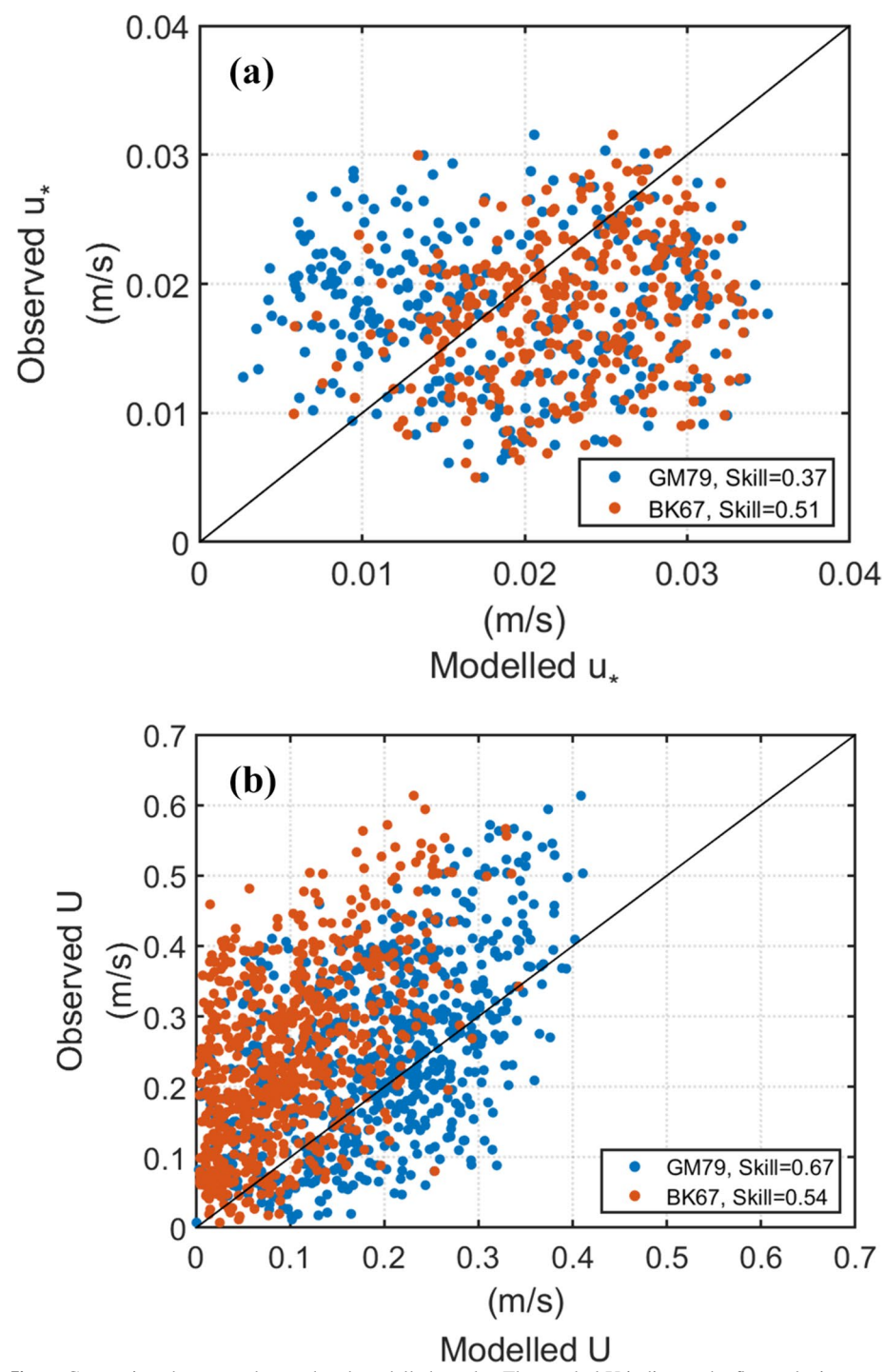


Fig. 7 Comparison between observed and modelled results. The symbol U indicates the flow velocity magnitude, and u_* indicates the bed shear velocity. a Scatter plot of u_* with legends of skill values. b Scatter plot of U with legends of skill values



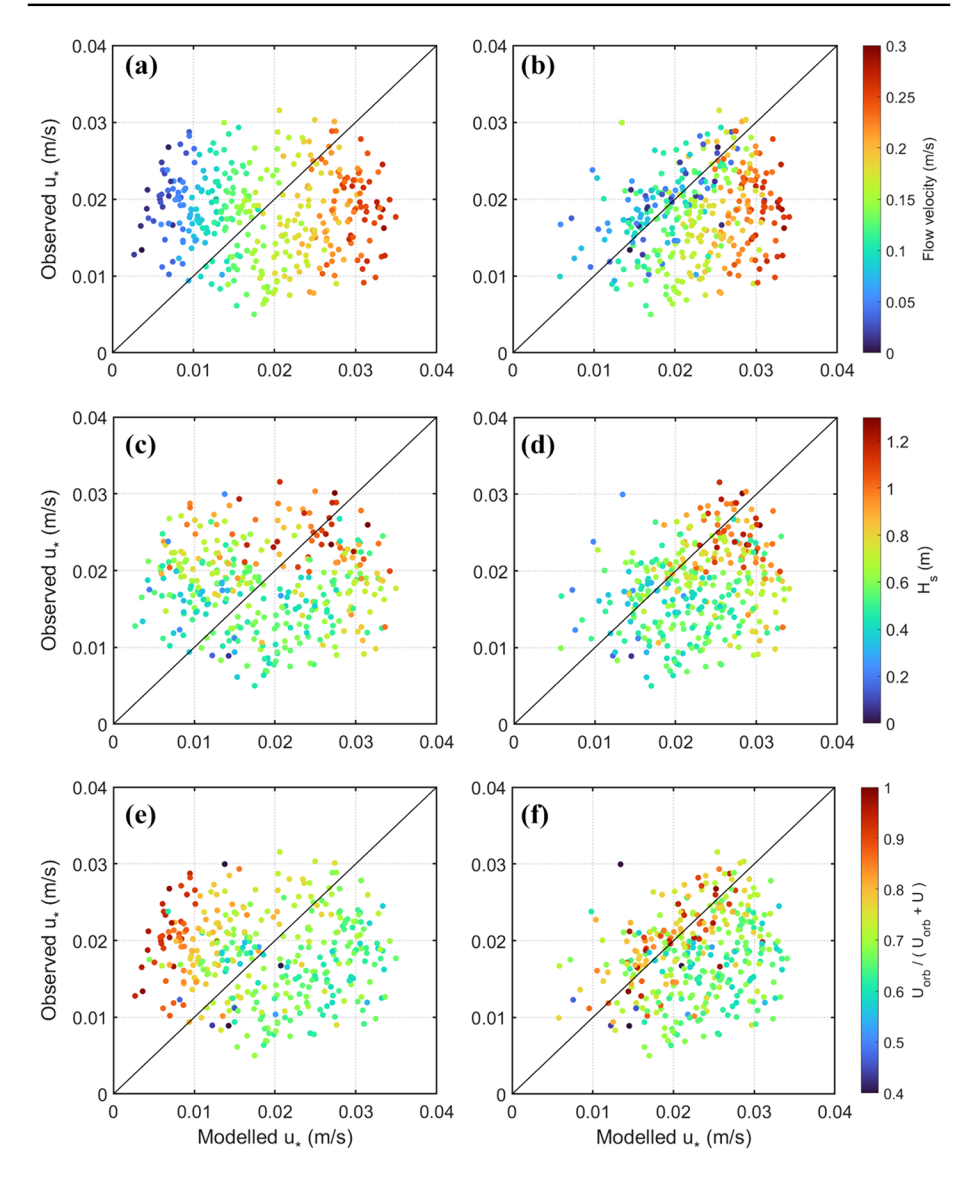


Fig. 8 Scatter plot of observed and modelled bed shear velocity (u_*) using $(\mathbf{a}, \mathbf{c}, \mathbf{e})$ GM79 and $(\mathbf{b}, \mathbf{d}, \mathbf{f})$ BK67 models. \mathbf{a} and \mathbf{b} are colored by flow velocity (U); \mathbf{c} and \mathbf{d} are colored by significant wave height; \mathbf{e} and \mathbf{f} are colored by the ratio of modelled wave orbital velocity (U_{orb}) to the sum of wave orbital velocity and flow velocity (U)

BK67. This suggests that the shear velocity at this study site is primarily influenced by waves, accounting for more than half of the values. The BK67 and GM79 models use different parameters to amplify the impact of wave-current interactions. Further discussions on these two models are provided below.

Scatter plots colored by parameters are shown in Fig. 8, including current magnitude (U), significant wave height, and the ratio of wave orbital velocity (U_{orb}) to the sum of



wave orbital velocity and current velocity. The data distribution in color shows a correlation with the modeled shear velocities (Fig. 8a). In GM79, the model tends to overpredict the shear velocity at high flow velocities while underpredicting at low flow velocities. This indicates that the bed shear velocity is dominantly subject to the current speed when using the GM79 model. Figure 8(b) shows overpredictions of shear velocities for higher current velocities, while most of the good agreement occurs at low current velocities when using the model of BK67. Figure 8(c) and (d) show that the agreement between the modeled and observed velocities does not correlate with the significant wave heights for using both models of GM79 and BK67.

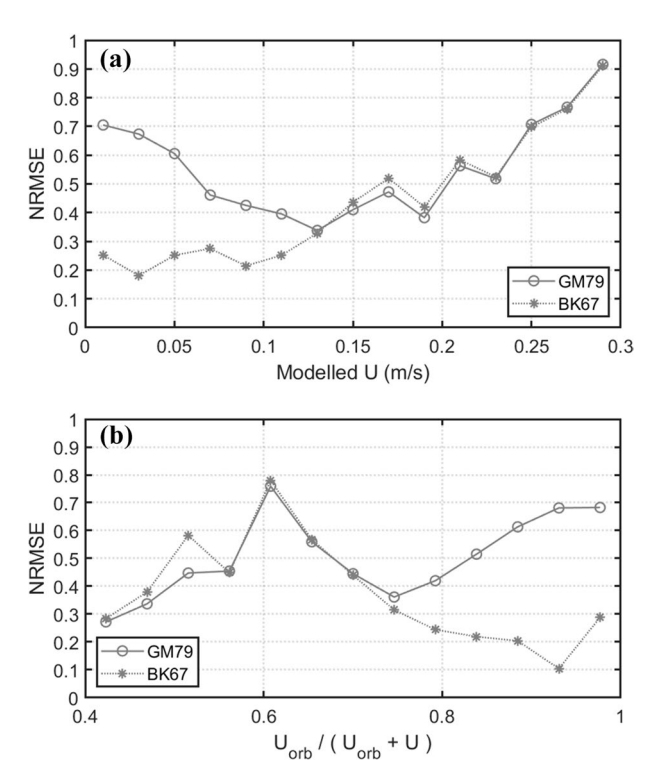
Results colored by the ratio of $U_{orb}/(U_{orb}+U)$ are shown in Fig. 8(e) and (f). The GM79 model underpredicts and overpredicts the shear velocities for higher and low values of U_{orb} , respectively. When increasing the nonlinear contribution of bed shear stress from waves with the model of BK67, the model accurately captures the bed shear velocities for higher U_{orb} .

The normalized root-mean-square error (NRMSE) between the modeled and observed results were computed as:

$$NRMSE = \sqrt{\frac{\sum (X_{simu} - X_{obs})^2}{\sum (X_{obs})^2}}.$$
 (9)

The NRMSEs between the observed and modeled shear velocities are plotted as a function of current magnitude U, as shown in Fig. 9. The NRMSEs increase at both lower

Fig. 9 Normalized-root-meansquared-error (NRMSE) between observed and modelled bed shear velocity(u*) as a function of **a** flow velocity (U), and **b** the ratio of modelled wave orbital velocity (U_{orb}) to the sum of wave orbital velocity and flow velocity (U)





and higher current speed when using the GM79 model (Fig. 9a); the NRMSEs decrease when the current speed decrease when using BK67 model. The significant difference in NRMSEs between GM79 and BK67 occurs at a current speed smaller than about 0.15 m/s. The NRMSEs are plotted as a function of $U_{orb}/(U_{orb}+U)$ as shown in Fig. 9(b). The NRMSEs in BK67 significantly decrease, and the difference between BK67 and GM79 increases when U_{orb} increases.

Modeling with different wave-current interaction methods reveals the importance of the nonlinear enhancement of shear stresses from waves. When the current speed is smaller than 0.15 m/s, the bed shear stresses are significantly enhanced by wave-current nonlinear interaction. The bottom roughness keeps constant in this study, and only parameters of the nonlinear interaction between wave-induced and current-induced bed shear stresses are different for the cases of using GM79 and BK67 models. The results actually show a significant difference between the two wave-current nonlinear interaction models in the observed and modeled bed shear velocities. The model well captures the magnitude, trends, and variability of bed shear stress on the rough reef. The two models, GM79 and BK67, taking account of nonlinear enhancement from waves with different combinations of parameters, result in performances on reproduction of the shear velocity. During high wave orbital motions, the higher contribution from waves is an important factor to enhance the bed shear velocity as the modelled results of BK67, and therefore lowers the model error. The result indicates that nonlinear interaction in wave-current flows plays a critical role in the bed shear stress variation on the reef system.

4 Conclusions

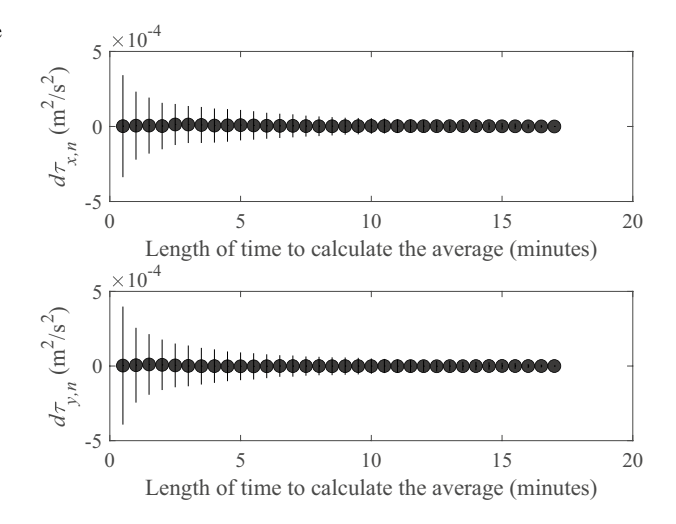
The depth-averaged currents and bed shear stresses over the algal reef on the Taoyuan coast were modeled using a coupled wave-current model. By comparing to field measurements obtained by the ADCP, the model driven by hydrodynamic forcing in terms of tides, waves, and wind stresses was validated. The current velocities, significant wave heights, and wave directions greatly agreed with field observations. The model results show that the current data oscillates with tides, indicating that tide is the primary factor driving the current in shallow waters. However, there is a discrepancy in model skills between flood and ebb tides, which manifests good predictions on current velocities during flood tides while underestimations during ebb tides; more studies and numerical testing are needed.

Two numerical tests with or without wind forcing indicate that the wind forcing significantly influences the depth-averaged currents. The model skills on current velocities show a slight difference between the two cases. The current speed is altered by wind according to the angle difference between the wind and the current. The current has a larger speed as it goes in the same direction as the wind, while the current speed tends to be smaller as it goes oppositely to the wind.

The model well captures the magnitude, trends, and variability of bed shear stress on the rough reef. Results from the two wave-current nonlinear interaction models reveal that the nonlinear contribution from waves might enhance the bed shear stress during high wave orbital motions. The result indicates that nonlinear interaction in wave-current flows might play an important role in the variation of bed shear stress on the reef system. Considering the parameterized physical processes, improvement of the present wave-current interaction model on predicting the bed shear stresses may be needed. This study provides new access



Fig. 10 Convergence tests on the length of time to calculate the average of measured turbulent shear stresses. Upper and lower panels are the cross-shore and alongshore components. The vertical bars are the standard deviation from 394 hourly burst measurements



to understanding the hydrodynamic processes with wave-current interaction on a coastal reef.

Appendix A: Error analysis on velocity and turbulence measurements

The measurement error of velocity and turbulent stresses by ADCP and ADV may be attributed to the accuracy of the instruments and the data analysis. The accuracy of the velocity measurement of ADCP and ADV is around $\pm 0.3\%$ and $\pm 0.5\%$ of the measured values, which gives an approximate error of 3 mm/s in velocity measurement.

To quantify the uncertainty of using different lengths of time to calculate the average of measured turbulence statistics, convergence tests for the time-averaged turbulent shear stresses were performed. Different lengths of time, n, were tested for calculating the time average cross-shore $(\tau_x = -u'w')$ and alongshore $(\tau_y = -v'w')$ turbulent shear stresses, and the relative error is defined as $d\tau_{y,n}$ and $d\tau_{y,n}$:

$$d\tau_{x,n} = \tau_{x,n} - \tau_{x,N}; n = 1, 2, ..., N,$$
(10)

$$d\tau_{y,n} = \tau_{y,n} - \tau_{y,N}; n = 1, 2, ..., N,$$
(11)

where n is the length of time for computing the time average and N = 17.67 min is the total length of time for averaging. The results indicate that the deviation is significant when the length of time for computing the time-averaging is smaller than 5 min as shown in Fig. 10. When the length of time for computing the averaging is greater than 10 min, the statistical value of turbulent shear stress will converge, indicating the burst measurement of 17 min is long enough to evaluate the turbulent statistics.

The setup of four ADVs allows us to evaluate the errors in separating the wave and turbulence components using the differencing technique. The cross-shore and alongshore turbulent shear stresses estimated at ADV1 were obtained by the differencing technique with ADV2, ADV3, and ADV4 as presented in Fig. 11. The results show that the error of



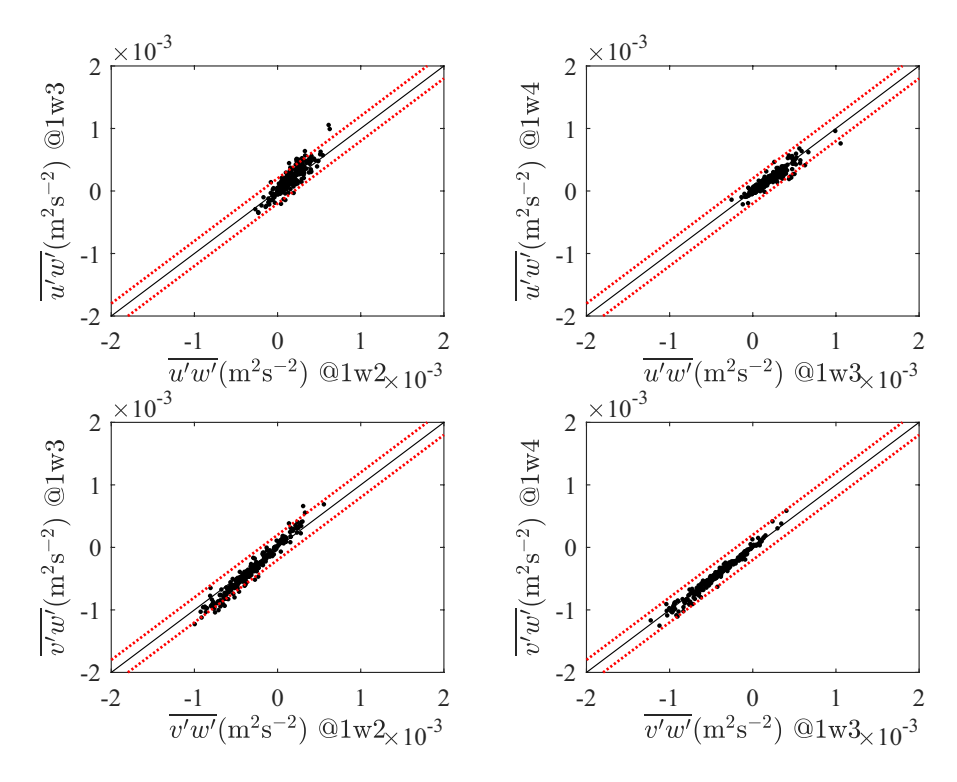


Fig. 11 Comparison of turbulent shear stresses obtained by differencing techniques with different vertical positions of ADVs. Diagonal lines are lines of equality. The left two panels are measurements at ADV1 by the differencing technique with ADV2 (symbol: @1w2) and ADV3(symbol: @1w3), respectively; right two panels are @1w3 and @1w4. The red dotted lines are 10% errors

Table 3 Coefficients of parameterizing bed shear stress in the wave-current interaction models

Model	a_1	a_2	a_3	a_4	\mathbf{m}_1	m_2	m_3	m_4
GM79	0.11	1.95	-0.49	-0.28	0.65	-0.22	0.15	0.06
BK67	0.00	2.00	0.00	0.00	0.00	0.50	0.00	0.00
Model	n ₁	n ₂	n ₃	n ₄	b ₁	b ₂	b ₃	b ₄
GM79	0.71	-0.19	0.17	-0.15	0.73	0.40	-0.23	-0.24
BK67	0.00	0.50	0.00	0.00	0.32	0.55	0.00	0.00
Model	p_1	p_2	p_3	p_4	q_1	q_2	q_3	q_4
GM79	-0.68	0.13	0.24	-0.07	1.04	-0.56	0.34	-0.27
BK67	-0.63	0.05	0.00	0.00	1.14	0.18	0.00	0.00



turbulent shear stress using the differencing technique with different vertical positions is mostly within 5%, and the maximum error may be around 10%.

Appendix B: Parameters in the wave-current interaction models

According to the approximation of Soulsby [54], each wave-current interaction method has its own fitting parameters, and each parameter (x = a, b, p, q, m, n) can be acquired from four minor parameters as:

$$x = (x_1 + x_2 |\cos \phi|^{\mathcal{I}}) + (x_3 + x_4 |\cos \phi|^{\mathcal{I}}) \log_{10} \frac{f_w}{C_{2D}}.$$
 (12)

The coefficients of parameterizing the bed shear stress in the wave-current interaction models are given in Table 3.

Acknowledgements The authors thank the three anonymous reviewers for their helpful comments and constructive suggestions to improve the original manuscript. Zhi-Cheng Huang was supported by the National Science and Technology Council in Taiwan under grant number NSTC 112-2621-M-008-004 and MOST108-2611-M-008-002. We thank CPC and the Office of Coast Administration Construction, Taoyuan City Government, for their long-term support in research funds from the granted projects.

Author contributions Yi-Ru Lan contributed to the implementation of the research, analysis of the results, and writing of the original manuscript. Zhi-Cheng Huang supervised the project and the study, designed the fieldwork, and improved and revised the manuscript. All authors discussed the results and contributed to the final manuscript.

Funding This research was supported by grants from the National Science and Technology Council in Taiwan under grant number NSTC 112-2621-M-008-004 and MOST108-2611-M-008-002.

Declarations

Conflict of interest The authors declare no competing interests.

Open Access This article is licensed under a Creative Commons Attribution 4.0 International License, which permits use, sharing, adaptation, distribution and reproduction in any medium or format, as long as you give appropriate credit to the original author(s) and the source, provide a link to the Creative Commons licence, and indicate if changes were made. The images or other third party material in this article are included in the article's Creative Commons licence, unless indicated otherwise in a credit line to the material. If material is not included in the article's Creative Commons licence and your intended use is not permitted by statutory regulation or exceeds the permitted use, you will need to obtain permission directly from the copyright holder. To view a copy of this licence, visit http://creativecommons.org/licenses/by/4.0/.

References

- Andrew J (1990) The physical oceanography of coral-reef systems. Ecosyst World, Coral Reefs 25:11-48
- Atkinson M, Smith SV, Stroup ED (1981) Circulation in enewetak atoll lagoon1. Limnol Oceanogr 26(6):1074–1083. https://doi.org/10.4319/lo.1981.26.6.1074
- Battjes, J. A. (1974). Computation of set-up, longshore currents, run-up and overtopping due to windgenerated waves.
- 4. Bijker, E. W. (1967). Some considerations about scales for coastal models with movable bed. *Publication. Delft Hydraulics Laboratory= Publikatie-Waterloopkundig Laboratorium*.



- Chang T-J, Wu Y-T, Hsu H-Y, Chu C-R, Liao C-M (2003) Assessment of wind characteristics and wind turbine characteristics in Taiwan. Renew Energy 28(6):851–871. https://doi.org/10.1016/S0960-1481(02)00184-2
- Chen X, Hara T, Ginis I (2020) Impact of shoaling ocean surface waves on wind stress and drag coefficient in coastal waters: 1. Uniform wind. J Geophys Res: Oceans 125(7):e2020JC016222. https://doi.org/10.1029/2020JC016222
- Davies AM, Lawrence J (1994) Examining the influence of wind and wind wave turbulence on tidal currents, using a three-dimensional hydrodynamic model including wave-current interaction. J Phys Oceanogr 24(12):2441–2460
- Davies AM, Lawrence J (1994) Modelling the non-linear interaction of wind and tide: its influence on current profiles. Int J Numer Methods Fluids 18(2):163–188. https://doi.org/10.1002/fld.1650180203
- Davis KA, Lentz S, Pineda J, Farrar J, Starczak V, Churchill J (2011) Observations of the thermal environment on Red Sea platform reefs: a heat budget analysis. Coral Reefs 30:25–36. https://doi.org/10.1007/s00338-011-0740-8
- De Goede ED (2020) Historical overview of 2D and 3D hydrodynamic modelling of shallow water flows in the Netherlands. Ocean Dyn 70(4):521–539. https://doi.org/10.1007/s10236-019-01336-5
- 11. Deltares (2021). D-Waves User Manual
- Douillet P, Ouillon S, Cordier E (2001) A numerical model for fine suspended sediment transport in the southwest lagoon of new Caledonia. Coral Reefs 20:361–372. https://doi.org/10.1007/ s00338-001-0193-6
- Drost EJF, Lowe RJ, Ivey GN, Jones NL (2018) Wave-current interactions in the continental shelf bottom boundary layer of the Australian North West Shelf during tropical cyclone conditions. Cont Shelf Res 165:78–92. https://doi.org/10.1016/j.csr.2018.07.006
- Dyer KR, Soulsby RL (1988) Sand transport on the continental shelf. Annu Rev Fluid Mech 20(1):295–324. https://doi.org/10.1146/annurev.fl.20.010188.001455
- Egan G, Cowherd M, Fringer O, Monismith S (2019) Observations of near-bed shear stress in a shallow, wave- and current-driven flow. J Geophys Res: Oceans 124(8):6323–6344. https://doi.org/10.1029/2019JC015165
- Grant WD, Madsen OS (1986) The continental-shelf bottom boundary layer. Annu Rev Fluid Mech 18(1):265–305. https://doi.org/10.1146/annurev.fl.18.010186.001405
- Green RH, Lowe RJ, Buckley ML (2018) Hydrodynamics of a tidally forced coral reef atoll. J Geophys Res: Oceans 123(10):7084–7101. https://doi.org/10.1029/2018JC013946
- Grimaldi CM, Lowe RJ, Benthuysen JA, Green RH, Reyns J, Kernkamp H, Gilmour J (2022) Wave and tidally driven flow dynamics within a coral reef atoll off northwestern Australia. J Geophys Res: Oceans 127(3):e2021JC017583. https://doi.org/10.1029/2021JC017583
- Gräwe U, Flöser G, Gerkema T, Duran-Matute M, Badewien TH, Schulz E, Burchard H (2016) A numerical model for the entire Wadden Sea: skill assessment and analysis of hydrodynamics. J Geophys Res: Oceans 121(7):5231–5251. https://doi.org/10.1002/2016JC011655
- Guo L, Qu K, Huang JX, Li XH (2022) numerical study of influences of onshore wind on hydrodynamic processes of solitary wave over fringing reef. J Mar Sci Eng 10(11):1645
- Holmedal LE, Wang H (2015) Combined tidal and wind driven flows and residual currents. Ocean Model 89:61–70. https://doi.org/10.1016/j.ocemod.2015.03.002
- Hsu W-Y, Huang ZC, Na B, Chang K-A, Chuang W-L, Yang R-Y (2019) Laboratory observation of turbulence and wave shear stresses under large scale breaking waves over a mild slope. J Geophys Res: Oceans. https://doi.org/10.1029/2019JC015033
- Huang Z-C, Lenain L, Melville WK, Middleton JH, Reineman B, Statom N, McCabe RM (2012) Dissipation of wave energy and turbulence in a shallow coral reef lagoon. J Geophys Res: Oceans. https://doi.org/10.1029/2011JC007202
- Huang Z-C, Yeh C-Y, Tseng K-H, Hsu W-Y (2018) A UAV–RTK lidar system for wave and tide measurements in coastal zones. J Atmos Ocean Technol 35(8):1557–1570. https://doi.org/10.1175/ JTECH-D-17-0199.1
- Huang ZC (2015) Vertical structure of turbulence within a depression surrounded by coral reef colonies. Coral Reefs 34:849

 –862. https://doi.org/10.1007/s00338-015-1304-0
- Hubbard A, Reidenbach M (2015) The effects of larval swimming behavior on the dispersal and settlement of the eastern oyster Crassostrea virginica. Mar Ecol Prog Ser. https://doi.org/10.3354/meps1 1373
- Jacob B, Stanev EV (2017) Interactions between wind and tidally induced currents in coastal and shelf basins. Ocean Dyn 67(10):1263–1281. https://doi.org/10.1007/s10236-017-1093-9
- Kuo C-Y, Keshavmurthy S, Chung A, Huang Y-Y, Yang S-Y, Chen Y-C, Chen C (2020) Demographic
 census confirms a stable population of the critically-endangered caryophyllid coral Polycyathus



- chaishanensis (Scleractinia; Caryophyllidae) in the datan algal reef, Taiwan. Sci Rep. https://doi.org/10.1038/s41598-020-67653-8
- Lý TN, Huang Z-C (2022) Real-time and long-term monitoring of waves and suspended sediment concentrations over an intertidal algal reef. Environ Monit Assess. https://doi.org/10.1007/s10661-022-10491-0
- Lesser GR, Roelvink JA, van Kester JATM, Stelling GS (2004) Development and validation of a threedimensional morphological model. Coast Eng 51(8):883–915. https://doi.org/10.1016/j.coastaleng. 2004.07.014
- Lim KY, Madsen OS (2016) An experimental study on near-orthogonal wave-current interaction over smooth and uniform fixed roughness beds. Coast Eng 116:258–274. https://doi.org/10.1016/j.coast aleng.2016.05.005
- Longuet-Higgins MS, Stewart RW (1962) Radiation stress and mass transport in gravity waves, with application to 'surf beats.' J Fluid Mech 13(4):481–504. https://doi.org/10.1017/S0022112062000877
- Lowe R, Leon A, Symonds G, Falter J, Gruber R (2015) The intertidal hydraulics of tide-dominated reef platforms. J Geophys Res: Oceans. https://doi.org/10.1002/2015JC010701
- Lowe RJ, Falter JL, Bandet MD, Pawlak G, Atkinson MJ, Monismith SG, Koseff JR (2005) Spectral wave dissipation over a barrier reef. J Geophys Res: Oceans. https://doi.org/10.1029/2004JC002711
- Lowe RJ, Falter JL, Monismith SG, Atkinson MJ (2009) A numerical study of circulation in a coastal reef-lagoon system. J Geophys Res: Oceans. https://doi.org/10.1029/2008JC005081
- Lowe RJ, Falter JL, Monismith SG, Atkinson MJ (2009) Wave-driven circulation of a coastal reeflagoon system. J Phys Oceanogr 39(4):873–893. https://doi.org/10.1175/2008JPO3958.1
- Luick JL, Mason L, Hardy T, Furnas MJ (2007) Circulation in the great barrier reef lagoon using numerical tracers and in situ data. Cont Shelf Res 27(6):757–778. https://doi.org/10.1016/j.csr.2006. 11.020
- MacVean LJ, Lacy JR (2014) Interactions between waves, sediment, and turbulence on a shallow estuarine mudflat. J Geophys Res: Oceans 119(3):1534–1553. https://doi.org/10.1002/2013JC009477
- Madsen OS, Poon Y-K, Graber HC (1988) Spectral wave attenuation by bottom friction: theory. Coast Eng Proc 1(21):34. https://doi.org/10.9753/icce.v21.34
- Manning, R. (1891). On the flow of water in open channels and pipes: Institute of Civil Engineers of Ireland Transactions, v. 20.
- 41. Mao M, van der Westhuysen AJ, Xia M, Schwab DJ, Chawla A (2016) Modeling wind waves from deep to shallow waters in lake michigan using unstructured SWAN. J Geophys Res: Oceans 121(6):3836–3865. https://doi.org/10.1002/2015JC011340
- Monismith SG (2007) Hydrodynamics of Coral Reefs. Annu Rev Fluid Mech 39(1):37–55. https://doi. org/10.1146/annurev.fluid.38.050304.092125
- Nielsen P (1992) Coastal bottom boundary layers and sediment transport, vol 4. World scientific, Singapore. https://doi.org/10.1142/1269
- 44. Pinazo C, Bujan S, Douillet P, Fichez R, Grenz C, Maurin A (2004) Impact of wind and freshwater inputs on phytoplankton biomass in the coral reef lagoon of New Caledonia during the summer cyclonic period: a coupled three-dimensional biogeochemical modeling approach. Coral Reefs 23:281–296. https://doi.org/10.1007/s00338-004-0378-x
- Reid EC, DeCarlo TM, Cohen AL, Wong GTF, Lentz SJ, Safaie A, Hall A, Davis KA (2019) Internal waves influence the thermal and nutrient environment on a shallow coral reef. Limnol Oceanogr 64(5):1949–1965. https://doi.org/10.1002/lno.11162
- Rijnsdorp DP, Buckley ML, da Silva RF, Cuttler MVW, Hansen JE, Lowe RJ, Green RH, Storlazzi CD (2021) A numerical study of wave-driven mean flows and setup dynamics at a coral reef-lagoon system. J Geophys Res: Oceans 126(4):e2020JC016811. https://doi.org/10.1029/2020JC016811
- Rogers JS, Monismith SG, Fringer OB, Koweek DA, Dunbar RB (2017) A coupled wave-hydrodynamic model of an atoll with high friction: mechanisms for flow, connectivity, and ecological implications. Ocean Model 110:66–82. https://doi.org/10.1016/j.ocemod.2016.12.012
- Ruessink BG, Houwman KT, Grasmeijer BT (2006) Modeling the nonlinear effect of wind on rectilinear tidal flow. J Geophys Res: Oceans. https://doi.org/10.1029/2006JC003570
- 49. Schlichting H, Gersten K (2016) Boundary-layer theory. Springer, Berlin, Heidelberg
- Shabani B, Nielsen P, Baldock T (2014) Direct measurements of wind stress over the surf zone. J Geophys Res: Oceans 119(5):2949–2973. https://doi.org/10.1002/2013JC009585
- Shaw WJ, Trowbridge JH (2001) The direct estimation of near-bottom turbulent fluxes in the presence of energetic wave motions. J Atmos Ocean Technol 18(9):1540–1557
- Shemer L, Singh SK, Chernyshova A (2020) Spatial evolution of young wind waves: numerical modelling verified by experiments. J Fluid Mech. https://doi.org/10.1017/jfm.2020.549



- Singh SK, Raushan PK, Debnath K (2018) Combined effect of wave and current in rough bed free surface flow. Ocean Eng 160:20–32. https://doi.org/10.1016/j.oceaneng.2018.04.055
- Soulsby RL (1995) Bed shear-stresses due to combined waves and currents. In: Advances in coastal morphodynamics. Delft Hydraulics, Netherlands, pp 4-20–4-23
- 55. Soulsby RL (1997) Dynamics of marine sands : a manual for practical applications. Thomas Telford
- Soulsby RL, Hamm L, Klopman G, Myrhaug D, Simons RR, Thomas GP (1993) Wave-current interaction within and outside the bottom boundary layer. Coast Eng 21(1):41–69. https://doi.org/10.1016/ 0378-3839(93)90045-A
- Swart, D. H. (1974). Offshore sediment transport and equilibrium beach profiles. Delft Hydraulics, Pub., 131.
- Trowbridge J, Lentz S (2018) The bottom boundary layer. Ann Rev Mar Sci 10:397–420. https://doi. org/10.1146/annurev-marine-121916-063351
- Van Dongeren A, Lowe R, Pomeroy A, Trang DM, Roelvink D, Symonds G, Ranasinghe R (2013) Numerical modeling of low-frequency wave dynamics over a fringing coral reef. Coast Eng 73:178– 190. https://doi.org/10.1016/j.coastaleng.2012.11.004
- Velioglu Sogut D, Sogut E, Farhadzadeh A (2021) Interaction of a solitary wave with an array of macro-roughness elements in the presence of steady currents. Coast Eng 164:103829. https://doi.org/ 10.1016/j.coastaleng.2020.103829
- Willmott CJ (1981) ON THE VALIDATION OF MODELS. Phys Geogr 2(2):184–194. https://doi.org/ 10.1080/02723646.1981.10642213
- Wu J (1975) Wind-induced drift currents. J Fluid Mech 68(1):49–70. https://doi.org/10.1017/S0022 112075000687
- 63. Yelland M, Moat B, Taylor PK, Pascal R, Hutchings J, Cornell VC (1998) Wind stress measurements from the open ocean corrected for airflow distortion by the ship. J Phys Oceanogr 28:1511–1526. https://doi.org/10.1175/1520-0485(1998)028%3c1511:WSMFTO%3e2.0.CO;2
- Young IR (1989) Wave transformation over coral reefs. J Geophys Res: Oceans 94(C7):9779–9789. https://doi.org/10.1029/JC094iC07p09779
- 65. Yu H-Y, Huang S-C, Lin H-J (2020) Factors structuring the macrobenthos community in tidal algal reefs. Mar Environ Res 161:105119. https://doi.org/10.1016/j.marenvres.2020.105119
- 66. Zhang X, Simons R, Zheng J, Zhang C (2021) A review of the state of research on wave-current interaction in nearshore areas. Ocean Eng 243:110202. https://doi.org/10.1016/j.oceaneng.2021.110202

Publisher's Note Springer Nature remains neutral with regard to jurisdictional claims in published maps and institutional affiliations.

